anomalies of 2 to 8 m/s. These results are consistent with those reported for other GCMs (*13, 14*) and are in the lower bound of measurements. By Eliasen-Palm (EP) flux diagnostics (*19*) it is possible to evaluate the acceleration of the mean zonal flow forced by the wave dissipation. In situations where weak eastward winds prevail in the Emeraude simulation at 10 hPa, the EP flux divergence for wave number 1 maximizes near the level of greater vertical wind shear in the stratosphere at and just above 30 km. The amplitude of the westerly acceleration computed from the EP flux divergence spreads over one or two model levels with values in the range 0.05 to 0.1 m/s per day. Thus, the acceleration produced by the model during transitions to the westerly phase of the QBO can be attributed to the absorption of the Kelvin waves, but a complete reversal of the zonal wind below 10 hPa would require additional forcing or larger absorption of the Kelvin waves in the lower stratosphere.

Rossby-gravity modes are also present in the simulations. A power spectra analysis applied on Emeraude model outputs shows a peak signal for westward-propagating waves with zonal wave number 4 to 5, a period ranging from 2.8 to 7 days, and maximum amplitude for the meridional component of the wind of about 2 to 3 m/s between 100 and 3 hPa. These values fall within the lower range of the observed values. Calculations of the EP flux divergence for these waves show that they exert an easterly acceleration on the mean flow that is broadly distributed over the stratosphere with a maximum of up to 0.1 to 0.2 m/s per day. This drag is balanced by the momentum transport from the mean meridional residual circulation.

We conclude that the Kelvin and Rossby-gravity equatorial waves, which are present in the simulations, are well enough developed to produce a QBO signal with an adequate time period and vertical phase propagation but that an additional forcing is required to produce a QBO that extends into the entire lower stratosphere with an amplitude of several tenths of meters. It is in particular the westerly acceleration that is too weak.

Additional energy for the Rossby-gravity waves could perhaps be obtained by increases in the vertical resolution of the models, but this is unlikely to be sufficient (*14*) and should act rather to increase the easterly winds. The horizontal truncation of the models is clearly adequate to resolve the large-scale Kelvin waves, but small-scale gravity waves with horizontal wavelengths smaller than about 1000 km are not resolved. The breaking of eastward-propagating gravity waves accounts for the westerly deceleration of the mesospheric equatorial jet during the westerly phase of the SAO. Such a mechanism could also be at play for the buildup of the westerly phase of the QBO. In particular, deceleration of the easterly flow by the gravity waves would increase the vertical wind shear and favor the occurrence of critical levels and the damping of Kelvin waves. The present models include a parameterization for the drag due to the breaking of the orographic gravity waves. Other sources of gravity waves, such as vertical wind shear and convection, could play an equally important role in the equatorial stratosphere.

The present study has demonstrated that a QBO signal can develop in GCMs. Further improvement in the representation of unresolved subgrid scale phenomena might be required to produce an oscillation with an amplitude and height comparable to the observed QBO.

REFERENCES AND NOTES

1. R. J. Reed, *J. Meteorol.* **12**, 226 (1955).
2. R. G. Veryard and R. Ebdon, *Meteorol. Mag.* **90**, 125 (1961).
3. R. H. Tolson, *J. Geophys. Res.* **86**, 7312 (1981).
4. F. Hasebe, *ibid.* **88**, 6819 (1983).
5. K. Labitkze and H. Van Loon, *J. Atmos. Terr. Phys.* **50**, 197 (1988).
6. R. R. Garcia and S. Solomon, *Geophys. Res. Lett.* **14**, 848 (1987).
7. J. R. Holton and R. S. Lindzen, *J. Atmos. Sci.* **29**, 1076 (1972).
8. W. J. Randel and J. C. Gille, *ibid.* **48**, 2336 (1991).
9. M. Yanai and T. Maruyama, *J. Meteorol. Soc. Jpn.* **44**, 291 (1966).
10. W. J. Randel, B. A. Boville, J. C. Gille, *J. Atmos. Sci.* **47**, 3092 (1990).
11. L. Gray and J. Pyle, in *Transport Processes in the Middle Atmosphere*, G. Visconti and R. Garcia, Eds. (Kluwer, Dordrecht, Netherlands, 1987), p. 199.
12. M. Takahashi and B. Boville, *J. Atmos. Sci.* **49**, 1020 (1992).
13. Y. Hayashi, D. G. Golder, J. D. Mahlman, *ibid.* **41**, 1971 (1984).
14. B. Boville and W. J. Randel, *ibid.* **49**, 785 (1992).
15. D. Cariolle, M. Amodei, P. Simon, *J. Atmos. Terr. Phys.* **54**, 627 (1992).
16. J.-F. Mahfouf, D. Cariolle, J.-F. Royer, *C. R. Acad. Sci. Ser. II* **316**, 61 (1993).
17. P. Courtier, C. Freydier, J.-F. Geleyn, F. Rabier, M. Rochas, in *Proceedings of the Workshop on "Numerical Methods in Atmospheric Models,"* Reading, England, 8 to 13 September 1991 (European Center for Medium-Range Weather Forecasts, Reading, England, 1992), p. 193.
18. B. Naujokat, *J. Atmos. Sci.* **43**, 1873 (1986).
19. D. G. Andrews and M. McIntyre, *ibid.* **33**, 2049 (1976).
20. The development of the models and the long-term simulations have been sponsored by the Programme Atmosphère Moyenne of the Centre National d'Etudes Spatiales, the Centre National de la Recherche Scientifique, and the Ministère de l'Environnement, by the Alternative Fluorocarbons Environmental Acceptability Study under contract CTR91-29/P91-078, and by the Commission of the European Communities, Environment Program. The Arpège–Integrated Forecast System code is a joint development of the European Center for Medium-Range Weather Forecasts and Météo-France.

18 March 1993; accepted 24 June 1993

Fabrication and Magnetic Properties of Arrays of Metallic Nanowires

T. M. Whitney, J. S. Jiang, P. C. Searson,* C. L. Chien*

Arrays of ferromagnetic nickel and cobalt nanowires have been fabricated by electrochemical deposition of the metals into templates with nanometer-sized pores prepared by nuclear track etching. These systems display distinctive characteristics because of their one-dimensional microstructure. The preferred magnetization direction is perpendicular to the film plane. Enhanced coercivities as high as 680 oersteds and remnant magnetization up to 90 percent have also been observed.

Artificially structured materials with nanometer-sized entities, such as superlattices and granular solids, have attracted much attention in recent years because of their distinctive properties and potential for technological applications (*1*). Their intricate properties are directly related to the low dimensionality of the entities and can be manipulated through the extra degrees of freedom inherent to their nanostructure. Whereas a bulk solid is three-dimensional, superlattices consist of two-dimensional entities of nanometer thicknesses. By manipulating the layer thickness, the properties of a superlattice can be drastically altered. For example, in magnetic multilayers (such as Fe/Cr and Co/Cu), the spin arrangement of the magnetic layers is dictated by the precise thickness of the nonmagnetic layers (*2, 3*). Equally interesting, in those multilayers where antiferromagnetic alignment of the magnetic layers is realized, giant magnetoresistance has been observed. Granular solids consist of nanometer-sized metallic particles (sometimes referred to as the zero-

---

T. M. Whitney and P. C. Searson, Department of Materials Science and Engineering, The Johns Hopkins University, Baltimore, MD 21218.
J. S. Jiang and C. L. Chien, Department of Physics and Astronomy, The Johns Hopkins University, Baltimore, MD 21218.

*To whom correspondence should be addressed.

dimensional entities) embedded in an immiscible medium (*4, 5*). By manipulating the size of the metallic particle and the metal volume fraction, a wide range of nanostructure-induced physical properties can be systematically varied and tailored. In this work, we describe a new type of artificially structured materials with one-dimensional entities. These materials consist of an array of metallic nanowires that are a few tens of nanometers in diameter. Their properties are intrinsically different from those of the other artificially structured materials mentioned above because the entities are one-dimensional. We report the fabrication and the anisotropic magnetic properties of arrays of Ni and Co nanowires.

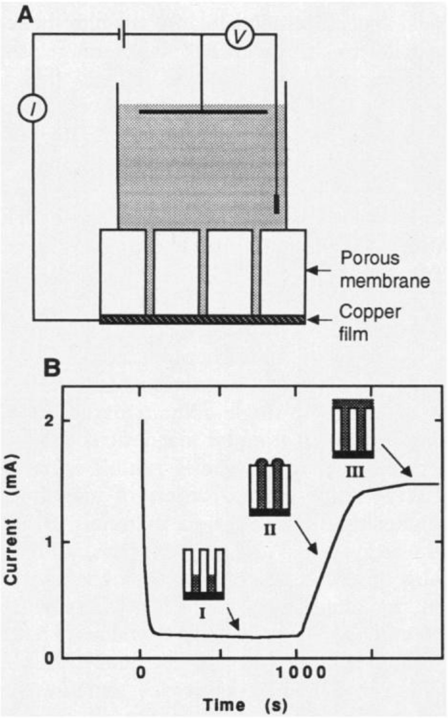

Fig. 1. (**A**) Schematic illustration of electrode arrangement for deposition of nanowires. (**B**) Current-time curve for electrodeposition of Ni into a polycarbonate membrane with 60-nm diameter pores at −1.0 V (versus Ag/AgCl). The insets depict the different stages of the electrodeposition as explained in the text.

Arrays of metallic nanowires were fabricated by electrochemical deposition of the material of interest into a template of nanometer-sized pores created by nuclear track etching. This technique was based on the work of Possin (*6*), who reported the fabrication of nanowires in mica, and the improvements reported by Williams and Giordano (*7*) during their study of electron localization in isolated Au nanowires. The basic process is that the rapid passage of heavy ions (such as those emitted from a radioactive transuranium isotope) through a dielectric material creates latent nuclear damage tracks (*8*). These zones of structural damage are much more chemically active than the undamaged material. A suitable etchant can preferentially dissolve the damaged zones with a very high selectivity (as high as 1000 to 1) compared to the undamaged regions for mica and some polymers, resulting in etched pores that can have extremely small lateral dimensions of a few tens of nanometers through the thickness of the dielectric (*9*). We used this method to fabricate porous polycarbonate membranes with circular pore cross section having diameters as small as 18 nm (*10*). The nanowires reported here, however, were fabricated by using Nuclepore polycarbonate membranes with diameters of 30, 60, 100, and 200 nm. These membranes are approximately 6 μm thick and have relatively high pore densities of $\sim 6 \times 10^8$ cm^{-2}.

In order to fabricate an array of nanowires, on one side of the polycarbonate membrane we first sputter-deposited a Cu film, which is the working electrode in a three-electrode electrochemical cell shown in Fig. 1A. The electrodeposition solution was confined to the bare side of the membrane so that deposition was initiated onto the Cu film from within the pores. In contrast to previous work, the electrodeposition was carried out at constant potential so that the deposition process could be monitored from the current response. Arrays of Ni and Co nanowires were deposited from nickel sulfamate solution (*11*) and Co(II) sulfate solution (*12*), respectively.

At any given potential, under the pseudo–steady-state conditions, the electrodeposition current was directly proportional to the area of the electrodeposit. Hence the current-time curves recorded during the electrodeposition process revealed various stages of the electrodeposition, as shown in Fig. 1B. After an initial transient, the current-time curve exhibited three distinct regions. Region I corresponds to the electrodeposition of metal into the pores in the membrane. Note that the presence of a supporting electrolyte minimizes diffusional effects in the pores. Region II results from the rapid increases in the deposition area that occurs when the pores are completely filled with the deposited metal and the electrodeposit begins to form hemispherical caps over the end of each nanowire. The formation of this structure causes an increase in the deposition current that continues until the caps coalesce into a planar and contiguous metallic top layer for which the current is now constant (region III). Thus, by stopping the electrodeposition process at the transition point between region I and II, an array of filled pores, or nanowires, is formed. The ratio of the deposition currents in regions I and III

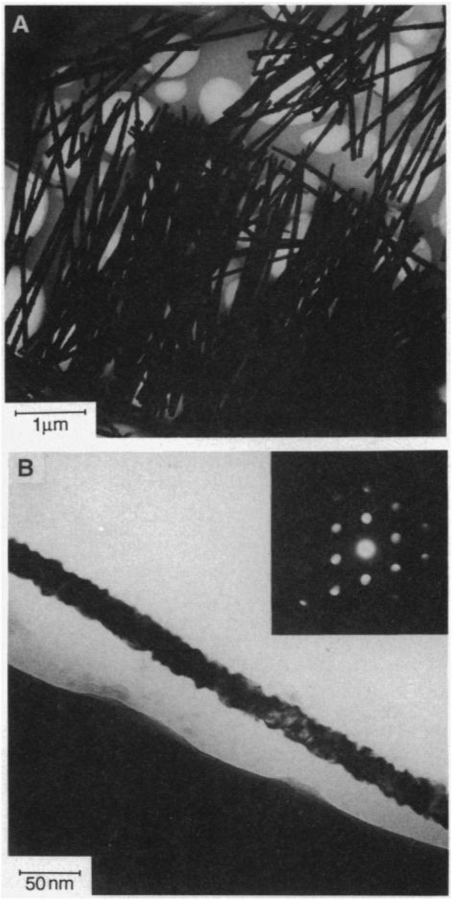

Fig. 3. (**A**) A TEM image of 60-nm diameter Ni nanowires after removal of the polycarbonate matrix. (**B**) Bright-field TEM image and electron diffraction pattern of a segment of a 30-nm diameter Ni nanowire.

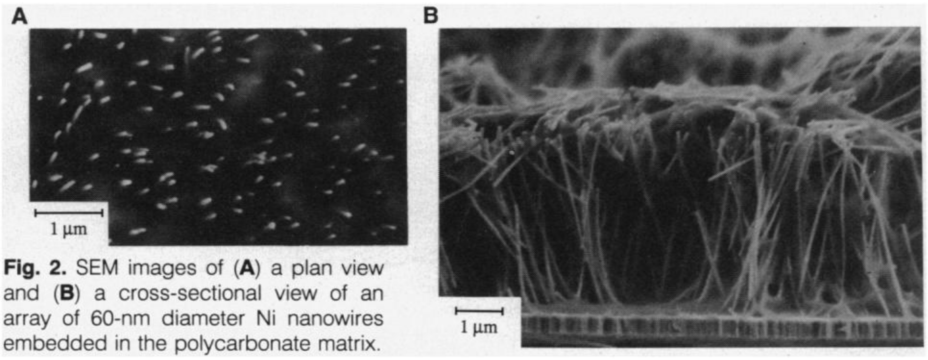

Fig. 2. SEM images of (**A**) a plan view and (**B**) a cross-sectional view of an array of 60-nm diameter Ni nanowires embedded in the polycarbonate matrix.

is equal to the ratio of the pore area to the geometrical area.

The morphology of the arrays of nanowires deposited in the membrane has been studied by using scanning electron microscopy (SEM). Figure 2A is a top-view SEM micrograph made after removing the top layer of the polycarbonate membrane with a suitable solvent and illustrates the random locations of the nanowires in the membrane. Figure 2B shows a cross section of a nanowire array after complete removal of the polycarbonate membrane. The nanowires are narrow and continuous, with length equal to that of the membrane (Fig. 2B).

The structure and morphology of the nanowires were examined by transmission electron microscopy (TEM) after dissolving the membrane. Figure 3A shows a number of 60-nm diameter Ni nanowires after removal from the polycarbonate membrane showing that this process can be used to fabricate large arrays of uniform and continuous wires. Figure 3B shows a 30-nm diameter Ni nanowire after removal from the membrane. Independent of the wire diameter, all samples exhibited surface roughness on the order of a few nanometers, which, although very small on a macroscopic scale, is a significant fraction of the wire diameter. Both Ni and Co nanowires were polycrystalline with grains generally extending the full width of the wire. The grain boundaries were usually aligned perpendicular to the growth direction at regular spacings, typically in the range of 5 to 50 nm or more, although in some cases the boundaries were aligned at an angle of ~45°. The electron diffraction pattern shown in Fig. 3B was obtained from an individual grain with a convergent beam and revealed the characteristic interplanar spacings of face-centered cubic Ni.

In most cases, the length of the grains decreased with increasing nanowire diameter, except when twin boundaries were present. In this case, nanowire segments were characterized by a series of periodic twin boundaries with a total length of many diameters. Examples of twin boundaries can be seen in the Ni nanowire shown in Fig. 3B.

The preferred growth directions for the nanowires were determined from comparison of the electron diffraction patterns and the corresponding electron micrographs. For the larger nanowires, the preferred growth orientation was the [111] direction for the Ni, and the [0001] direction for the Co nanowires. From examination of many wires, however, a number of other orientations were observed, particularly for the smaller diameter wires.

Because the arrays of nanowires are made of ferromagnetic Co or Ni, an immediate and necessary consequence is the realization of anisotropic magnetic properties. For a ferromagnetic thin film, the layer geometry dictates that the demagnetizing factors be approximately 0 and 4π for fields parallel and perpendicular to the film plane, respectively (13). Consequently, the shape anisotropy tends to force the magnetization M to be in the film plane. It takes an external field of at least $4\pi M$ to align M perpendicular to the film plane. However, it is highly desirable, particularly in perpendicular magnetic recording, to have M perpendicular to the film, a situation unfavored by the shape anisotropy. Attempts to overcome this difficulty include exploiting the special magnetocrystalline anisotropy and magnetic surface anisotropy (14) of some magnetic materials or taking advantage of the naturally occurring columnar structure in certain magnetic thin films, such as sputter-deposited Co-Cr alloys (15).

For a rod-shaped ferromagnetic entity, the demagnetizing factors for fields applied along and perpendicular to the rod axis are approximately 0 and 2π, respectively. In the absence of an external field this shape anisotropy compels the magnetization to be along the axial direction. However, in the nanowire arrays, M along the nanowire direction leads to magnetization perpendicular to the membrane or sample plane. In other words, the highly desirable but elusive perpendicular magnetization is a natural consequence of the geometry of the ferromagnetic nanowire arrays.

Experimentally, the perpendicular magnetization of the nanowire arrays can be ascertained by magnetometry measurements with the external field applied perpendicular to the film plane ($H_\perp$, hence parallel to the nanowires) and parallel to the film plane ($H_\parallel$, hence perpendicular to the nanowires). The measurements were performed at room temperature with a vibrating sample magnetometer. The hysteresis curves of an array of Co nanowires with an average diameter of 60 nm are shown in Fig. 4. The "easy axis" is for the field applied perpendicular to the film, hence parallel to the nanowires. Furthermore, the saturation field for the parallel field ($H_\parallel$) is ~8400 Oe greater than that of the perpendicular field ($H_\perp$). This value is in excellent agreement with the demagnetizing field of $2\pi M$ = 8800 Oe for a thin Co rod. For arrays of Ni nanowires, the observed saturation field difference of 3000 Oe is also in good agreement with the value of $2\pi M$ = 3050 Oe. These results attest to the one-dimensional structure in the nanowire arrays.

Ultrafine ferromagnetic particles exhibit greatly enhanced magnetic coercivity because of their single-domain nature (13). Indeed, many granular magnetic solids and isolated ultrafine particles exhibit coercivities as much as two orders of magnitude higher than those of bulk materials (5). In the arrays of Co and Ni nanowires, we have also observed much enhanced coercivities in the range from 150 to 680 Oe, which should be compared with the values of a few tens of oersteds for bulk Ni and Co. The enhancement of coercivities increases for decreasing wire diameter (Fig. 5). This is

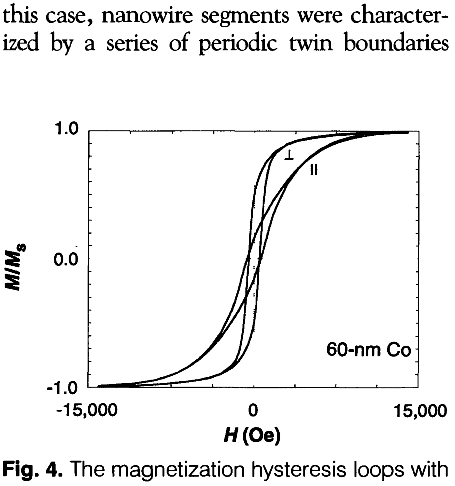

Fig. 4. The magnetization hysteresis loops with the magnetic field applied parallel (∥) and perpendicular (⊥) to the film plane for an array of 60-nm Co nanowires.

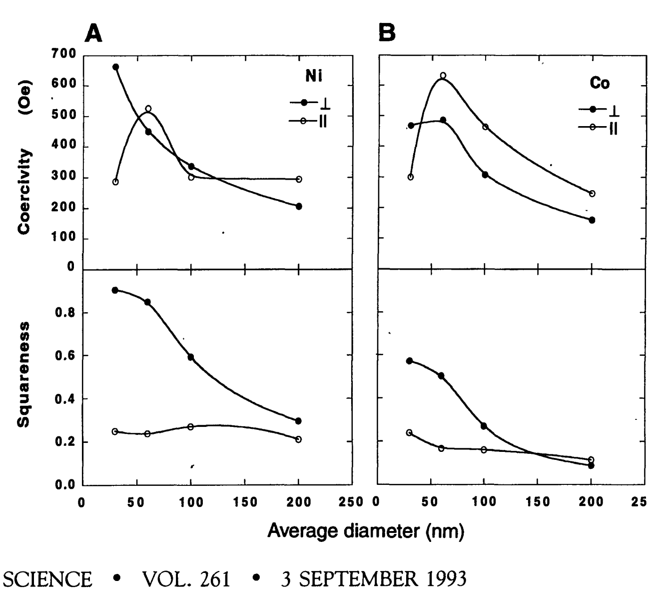

Fig. 5. The variation of coercivity and squareness with the average diameter of (**A**) Ni and (**B**) Co nanowire arrays. The data for parallel and perpendicular configurations are represented by open and closed circles, respectively.

expected because larger wire diameter facilitates the formation of multidomains, hence degrading the coercivity. For wire diameters less than 50 nm, the coercivity in some cases becomes smaller. This decrease may be due to the imperfections in the nanostructure. These results also suggest that coercivity can be further enhanced by improving the process for fabricating wires with diameter less than 50 nm.

Perpendicular magnetic recording has been a field under intense exploration. By having their preferred magnetization perpendicular to the film plane, magnetic media with perpendicular anisotropy can allow a smaller bit size to be used and thus increase the recording density (*15*). For a magnetic medium, it is desirable that it be resistant to magnetization reversal, that is, the coercivity should be moderately large. It is also desirable that the remnant magnetization (the magnetization that persists even when the field is absent) be large. As shown in Fig. 4, the magnetic nanowire arrays studied in this work exhibit high perpendicular anisotropy because of their artificial structure. In Fig. 5, we plot the wire diameter dependence of the squareness, which is the ratio of the remanence to saturation magnetization. As expected, the perpendicular squareness is much larger than the parallel squareness. In the case of both Co and Ni nanowires, the perpendicular squareness increases as the wire diameter decreases. The 30-nm Ni nanowire array retains as much as 90% of the magnetization at zero field. The high remanence, together with large coercivities, may make these materials useful for high-density perpendicular recording.

The significance of artificially created one-dimensional structures is much more far reaching than the novel magnetism of the magnetic nanowires studied in this work. One-dimensional structures composed of other suitable materials can also be anticipated to exhibit characteristics of both fundamental (*7*) and practical (*16*) interest.

REFERENCES AND NOTES

1. See, for example, P. Dhez and C. Weisbuch, Eds., *Physics, Fabrication, and Applications of Multilayer Structures* (Springer, Berlin, 1990).
2. M. N. Baibich *et al.*, *Phys. Rev. Lett.* **61**, 2472 (1988).
3. S. S. P. Parkin, N. More, K. P. Roche, *ibid.* **64**, 2304 (1990).
4. B. Abeles, in *Applied Solid State Science: Advances in Materials and Device Research*, R. Wolfe, Ed. (Academic Press, New York, 1976), pp. 1–117, and references therein.
5. C. L. Chien, *J. Appl. Phys.* **69**, 5267 (1991), and references cited therein.
6. G. E. Possin, *Rev. Sci. Instrum.* **41**, 772 (1970).
7. W. D. Williams and N. Giordano, *Phys. Rev. B* **33**, 8146 (1986).
8. B. E. Fischer and D. Spohr, *Rev. Mod. Phys.* **55**, 907 (1983); R. L. Fleischer, P. B. Price, R. M. Walker, *Nuclear Tracks in Solids Principles and Applications* (Univ. of California Press, Berkeley, 1975).
9. P. B. Price and R. M. Walker, *J. Appl. Phys.* **33**, 3407 (1962).
10. T. M. Whitney, thesis, Johns Hopkins University (1992).
11. The nickel was electrodeposited from the following solution: 20 g/liter $NiCl_2 \cdot 6H_2O$, 515 g/liter $Ni(H_2NSO_3)_2 \cdot 4H_2O$, and 20 g/liter H_3BO_3; pH 3.4.
12. The cobalt was electrodeposited from 252 g/liter $CoSO_4 \cdot 7H_2O$, 7 g/liter NaCl, and 50 g/liter H_3BO_3; pH 3.6.
13. See, for example, A. H. Morrish, *The Physical Principles of Magnetism* (Wiley, New York, 1965).
14. For a recent review, see U. Gradmann, *J. Magn. Magn. Mater.* **54–57**, 733 (1986).
15. S. Iwasaki and K. Ouchi, *IEEE Trans. Magn.* **MAG-13**, 1272 (1977).
16. M. Shiraki, Y. Wakui, T. Tokushima, N. Tsuya, *ibid.* **MAG-21**, 1465 (1985); N. Tsuya *et al.*, *ibid.* **MAG-22**, 1140 (1986); K. I. Arai, Y. Wakui, K. Ohmori, T. Tokoshima, *ibid.* **MAG-23**, 2245 (1987).

17. We gratefully acknowledge the assistance of J. M. Macaulay in providing the SEM images. This work was supported by the National Science Foundation under grant ECS 92-02222.

14 April 1993; accepted 12 July 1993

DNA Conformation–Induced Activation of an Enediyne for Site-Specific Cleavage

Lizzy S. Kappen and Irving H. Goldberg*

Neocarzinostatin chromophore (NCS chrom) was found to induce site-specific cleavage at the 3′ side of a bulge in single-stranded DNA in the absence of thiol. This reaction involved the oxidative formation of a DNA fragment with a nucleoside 5′-aldehyde at its 5′ terminus and generated an ultraviolet light–absorbing and fluorescent species of post-activated drug containing tritium abstracted from the carbon at the 5′ position of the target nucleotide. The DNAs containing point mutations that disrupt the bulge were not cleavage substrates and did not generate this drug product. Thus, DNA is an active participant in its own destruction, and NCS chrom may be useful as a probe for bulged structures in nucleic acids.

Neocarzinostatin chromophore (NCS-chrom) (*1*), like the other enediyne anticancer antibiotics calicheamicin (*2*), esperamicin (*3*), and kedarcidin (*4*), is activated for the cleavage of duplex DNA by reaction with thiol. Nucleophilic addition of thiol at C-12 of NCS-chrom (Fig. 1A) results in cycloaromatization of the drug through a Bergman-type reaction to generate the diradical species (*5*). Sequence-specific hydrogen atom abstraction by the diradical from the C-5′, C-1′, or C-4′ positions of deoxyribose in the minor groove of double-stranded (ds) DNA ultimately leads to strand cleavage (*1*). This cleavage is at least 1000 times greater in the presence of thiol than in its absence. Single-stranded (ss) DNA is not a substrate for thiol-activated enediynes except, as shown for NCS-chrom, where regions of ds structure can be generated intramolecularly (*6, 7*). Here, we report that a ssDNA that contains a bulge is cleaved efficiently and in a site-specific manner by NCS-chrom in the absence of activating thiol; a new drug product results from this reaction.

We found that treatment of ssDNA that corresponded to the 3′ terminus of yeast transfer RNA (tRNA^{Phe}) (31-I; Fig. 1B) with NCS-chrom in the absence of thiol (*8*) resulted in cleavage at a single site, T22 (Fig. 2A). This observation suggested that the radical form of NCS-chrom acts monofunctionally in cleaving the DNA. By contrast, dsDNA was not cleaved under these conditions. In the presence of thiol, NCS-chrom induced breaks in both ds- and ssDNAs, predominantly at T and A residues. The mobility of the T22 band in relation to chemical markers and its reduced mobility after exposure to the 3′-phosphatase activity of polynucleotide kinase suggested that the DNA fragment contained a 3′ terminal phosphate. Cleavage was not enhanced by piperidine treatment. Thiol-independent cleavage at T22 in the ss 31-I DNA was dependent on O_2; in its absence, a product (presumably a DNA-drug adduct) that migrated slower than the starting material was formed in an amount comparable to the amount of cleavage product formed in the presence of O_2 (*9*). Thus, drug activation takes place anaerobically, but cleavage of the DNA is an oxidative reaction.

The chemistry of damage at the 5′ end of the break at T22 in the thiol-independent reaction was revealed in experiments with 3′ ^{32}P-labeled ss 31-I (Fig. 2B). Treatment with NCS-chrom produced a band with electrophoretic mobility characteristics consistent with those of a DNA fragment that contained a nucleoside 5′-aldehyde at its 5′ end. Thus, the predominant band (a) moved 3.5 nucleotides more slowly than the

---

Department of Biological Chemistry and Molecular Pharmacology, Harvard Medical School, Boston, MA 02115.

*To whom correspondence should be addressed.